Thin–Walled Structures 155 (2020) 106941

Contents lists available at ScienceDirect

Thin-Walled Structures

journal homepage: http://www.elsevier.com/locate/tws

Responses of concrete-filled FRP tubular and concrete-filled FRP-steel double skin tubular columns under horizontal impact

Zhilin Chen[a], Jun Wang[a,*], Jiye Chen[b], Hota GangaRao[c], Ruifeng Liang[c], Weiqing Liu[a]

[a] College of Civil Engineering, Nanjing Tech University, Nanjing, People's Republic of China
[b] School of Civil Engineering and Surveying, University of Portsmouth, UK
[c] Department of Civil and Environmental Engineering, West Virginia University, WV, USA

ARTICLE INFO

Keywords:
Glass fiber-reinforced polymer (GFRP) tubes
Concrete
Steel tubes
Horizontal impact
Analytical method
FE model

ABSTRACT

This paper presented the experimental and analytical results of concrete-filled fiber-reinforced polymer (FRP) tubes (CFFTs) and concrete filled GFRP-steel double skin tubular columns (DSTCs) under horizontal impact loads. The influences of the thickness of FRP tubes and impact velocity were discussed. The thickness of the FRP tubes had insignificant influence for both the peak impact force and the maximum displacement. Under the same applied impact energy, the maximum displacement of concrete filled FRP-steel DSTC specimens was ~40% smaller than that of CFFT specimens. The impact velocity had more influence on the peak impact force than the duration. Three-dimensional finite-element (FE) models were developed to simulate the impact behavior of two types of composite columns and the numerical results are compared with the test data. Then, the verified FE model was used to conduct parametric study. Moreover, analytical solutions for lateral displacement of composite columns under impact were obtained, in which the effect of impact damage was considered by introducing reduction factors into the vibration equations. The comparison between analytical results and test results showed that the maximum displacement can be accurately predicted by the proposed theoretical model.

1. Introduction

Concrete filled fiber reinforced polymer (FRP) tubes (CFFTs) have been increasingly used as bridge piers, piles and fender systems because of their excellent behavior on load carrying capacity and ductility [1–3]. The outer FRP tube not only provides the concrete core with a stay-in-place formwork during construction, but also provides hoop confinement which results in enhancement in concrete compressive strength. Moreover, FRP tubes help protecting concrete insulate from aqueous corrosion. Simultaneously, FRP-concrete steel double-skin tubular columns (DSTCs) proposed by Teng et al. [4] are found to provide lighter self-weight, increase in section modulus, enhance stability and improve cyclic performance. DSTCs have prospective applications in structures such as bridges, high-rise buildings, viaducts and electricity transmission towers; hence the proposed approach is important for designers of such structures. Both CFFTs and FRP-concrete steel DSTCs are susceptible to lateral impact from vehicles and vessels. However, few studies have been conducted to explore the impact behavior of hybrid composite columns. The literature is replete with studies on bearing capacity of concrete columns wrapped with FRP under axial compression [5,6], bending [7,8], and cycling loading [9].

Recently, researchers have been investigating the impact responses of hybrid composite columns, i.e., concrete-filled FRP tubes and FRP-steel tubes, as well as FRP-concrete steel DSTCs. Pham and Hao [10] investigated the confinement mechanism of FRP confined columns under axial impacts. The rupture strain of glass fiber reinforced polymer (GFRP) was higher than that of carbon fiber reinforced polymer (CFRP), resulting in higher confinement efficiency of GFRP under impacts [10]. Qasrawi et al. [11] investigated the dynamic behavior of CFFTs under lateral impact. Their test results indicated that the outer GFRP tube contributed to sharply increase the impact resistance and energy absorption, compared with the unconfined counterparts. Moreover, a single degree of freedom model was developed by Qasrawi et al. [11] to predict the displacement histories CFFTs under impact, in which the damping and strain rate effects were considered. The studies of Huang et al. [12,13] showed that with the increase of impact energy, the peak impact force of CFFTs with steel spiral reinforcement changed insignificantly, while the duration increased slightly.

For concrete-filled steel tubes (CFSTs) wrapped with FRP, Xiao and Shen [14] studied the responses of CFSTs wrapped with CFRP under

---

* Corresponding author.
E-mail address: wangjun3312@njtech.edu.cn (J. Wang).

https://doi.org/10.1016/j.tws.2020.106941
Received 1 February 2020; Received in revised form 17 May 2020; Accepted 23 June 2020

axial impact. The impact force versus time histories for CFSTs wrapped with CFRP were similar to those of CFSTs, and increasing the number of layers of CFRP resulted in enhancing the peak impact force and duration [14]. Alam et al. [15] developed a finite element (FE) model to investigate the effect of bond length on the responses of CFRP strengthened CFTs under lateral impact. Their numerical results indicated that adhesive with high interfacial fracture energy contributed to minimize the lateral displacement of the CFSTs wrapped with CFRP under impact. Moreover, the effective bonding length of a CFRP strengthened CFST column to resist impact load was influenced by the impact energy, CFRP properties, adhesive type and axial loading level [15]. The impact tests of CFSTs wrapped with FRP conducted by Chen et al. [16] confirmed that GFRP confined tubes absorbed more energy and had smaller deflection than the CFRP confined tubes.

Limited studies have been conducted on the impact behavior of FRP-concrete steel DSTCs. Abdelkarim and ElGawady [17] conducted a parametric study of FRP-concrete steel DSTC columns under vehicle collisions by LS-DYNA software. They stated that the peak impact force of FRP-concrete steel DSTC column was lower than that of the RC column by approximately 40% and 28% when it was impacted by a vehicle with a mass of 2 ton at a velocity of 70 mph and 50 mph. Wang et al. [18] carried out experimental study on FRP-concrete steel DSTC columns under lateral impact. Their test results indicated that the impact force history of FRP-concrete steel DSTCs was similar to that of concrete filled steel tubes and concrete filled double steel tubes (CFDSTs). Fracture of the FRP jackets and crushing of filled concrete dominated the failure of the FRP-concrete steel DSTCs under impact. However, shear failure of the outer steel tube dominated the failure of CFDSTs [18].

Drop weight impact testing is the most common test to evaluate impact data of composite structures, which most closely resembles impact damage in the field. It has the advantage of having inherent fail-safe characteristics when the test specimens are destroyed completely, as the vertical motion of the hammer can be impeded by anvil seated on the string floor [19]. The authors have conducted drop weight impact testing on hybrid composite columns, i.e. hollow and concrete filled GFRP tube columns [20], bare steel tubes, as well as hollow steel tubes wrapped with GFRP [21], to investigate their responses subjected to lateral impact. The peak impact forces of CFFTs were much higher than those of hollow GFRP tubes, whereas the hollow GFRP tubes exhibited almost the same energy absorption capacities as CFFTs under the same magnitude of impact energy [20]. The prevalent damages in the hollow steel tubes were elephant's foot buckling at the clamped end and inwards at the loading point. However, shear failure of GFRP occurred at the clamped end of steel tubes wrapped with GFRP [21]. In drop weight impact system, the dropping hammer impacts the specimens vertically, and shall separate with the specimens promptly. Otherwise, the impactor will move together with the test specimens. In this event, it is necessary to take into account the effects of the additional mass on the impact responses of specimens. Moreover, it requires increasing the applied impact energy by increasing the height of the free fall or the dropping weight which implies increasing the height of the tower or strengthening the vertical guiding columns [22]. To overcome the shortcomings of drop weight impact system, horizontal impact system is developed to conduct impact test on structures. Aghdamy et al. [22] presented an experimental investigation on CFDSTs under the combined static axial loading and lateral impact loading. Their experiments were conducted on a new innovative horizontal impact testing system (HITS) which rig included a pneumatic instrumented striker, an axial pre-loading frame, a specimen supports system, a control box and data measuring instruments. The maximum applied impact energy and axial load of this HITS are 10.40 kJ and 1390 kN, respectively [22]. However, the drop weight impact testing system and the mentioned HITS are difficult to simulate the vehicle collision due to their limited applied impact energy capacity.

The objective of the present work is to investigate the impact behavior of CFFTs and FRP-concrete steel DSTCs using a horizontal trolley traction system. This system can reproduce full-scale crash tests. The effect of wall thickness of outer FRP tubes coupled with impact velocity is discussed, and then the failure modes and impact responses of CFFTs are compared with those of FRP-concrete steel DSTCs. FE models are constructed to conduct parametric study. Based on the theory of vibration of continuous beams, analytical dynamic response models are developed in which the impact load is simulated using a linear function and an exponential function. Finally, the proposed analytical model is verified using tested results.

2. Experimental program

2.1. Materials

The filament-wound GFRP tubes are made of isophthalic polyester resin with unidirectional E-glass fibers at ±55° winding angle with respect to the axial direction of the tube. The amount of resin volume percent is maintained close to 0.7. The tubes mechanical properties obtained from the manufacturer are: compressive strength 161 MPa, compressive modulus 12 GPa, Poisson's ratio 0.3, tensile strength 120 MPa, and tensile modulus 12.5 GPa given in the axial direction, and tensile strength 250 MPa, tensile modulus 22 GPa and a Poisson's ratio 0.22 given in the hoop direction.

Cold-formed Q235 steel tubes are used in the construction of concrete filled GFRP-steel double skin tubular columns. Tensile tests are conducted following the GB/T 228.1–2010 [23] to measure the material properties of the steel tubes. 0.2% proof stress of the steel is adopted as the yield stress. The test results showed that the steel tube has a yield stress of 278 MPa, Young's modulus of 201 GPa and Poisson's ratio of 0.3.

The filled concrete is from the same batch. Five 150 mm cubes are cast and cured under the conditions similar to the related columns. The compressive test results showed that the concrete has a compressive strength of 28 MPa, Young's modulus of 28 GPa and Poisson's ratio of 0.2.

Each specimen has a steel reinforced concrete abutment to fix the end of the column with the ground. The abutment is designed following the spread footing in GB 50007–2011 [24]. HRB 400 steel rebars are used as reinforcement in concrete of the abutments. All the specimens and abutments are cast from the same batch of concrete, as shown in Fig. 1(a). The abutment is fixed with the concrete floor by four steel bolts with diameter of 45 mm and length of 800 mm. The fabricating process includes: 1) installing the timber formwork of the abutment; 2) assembling the steel rebars in the abutment; 3) fixing the GFRP tubes and steel tubes (only for DSTCs) with the steel rebars and 4) casting concrete in the columns and abutments. Fig. 1 shows the fabrication process of the specimens.

2.2. Test specimen

Eight specimens are prepared to study structural responses under impact loads, in which four specimens are concrete filled FRP tubular columns (CFFTs), and the others are concrete filled FRP-steel DSTCs. 3. The filament-wound FRP tube is preferred by CFFTs, while the FRP tube with majority of fibres in the hoop direction is preferred by concrete filled FRP-steel DSTCs. To compare the impact responses of different types of composite columns under the same conditions, the filament-wound FRP tube is applied in CFFTs and concrete filled FRP-steel DSTCs in this investigation. All the test specimens have the same height (1560 mm) and GFRP inner diameter (300 mm). The side length of the reinforced concrete abutment with a square cross section is 900 mm. The maximum diameter of the column is determined to avoid the shear failure of the abutment, thus the outer diameter of the concrete core is 300 mm. The thickness of GFRP tubes is taken as 7 mm and 10 mm, respectively, and the outer diameter and thickness of the steel tubes are taken as 140 mm and 3 mm, respectively. Table 1 shows the impact

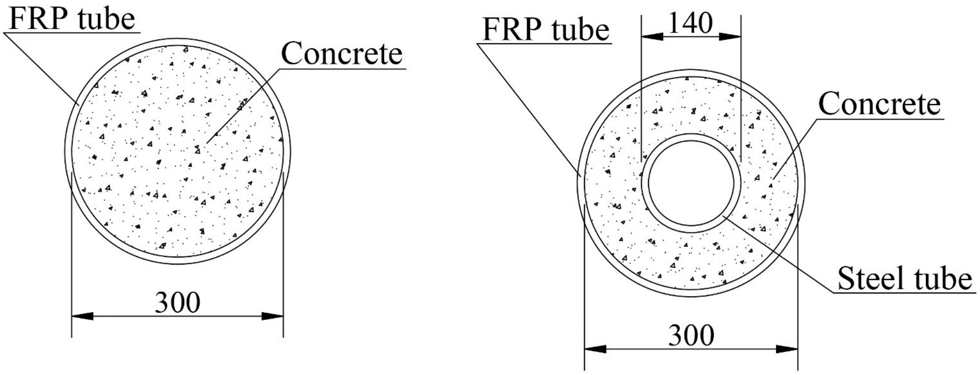

(a) Cross section of CFFTs

(b) Cross section of concrete filled FRP-steel DSTCs

(c) Assembling reinforcement of abutments

(d) Concrete placement

(e) Finished specimens

Fig. 1. Cross section and fabrication of specimens (unit: mm).

velocity and response data for all test specimens, including nomenclature abbreviations.

2.3. *Experimental set-up*

Impact systems, installed at the Advanced Engineering Composites Research Center at Nanjing Tech University, China, consist of a vertical drop weight and a horizontal trolley traction impact test machine, as shown in Fig. 2. The details of the vertical drop weight system have been reported by Wang et al. [20]. The horizontal trolley traction system is used to test the impact behavior of CFFTs and concrete filled FRP-steel DSTCs. The horizontal impact system consists of reaction wall, guide rail and trolley traction device. The mass of the trolley is 1580 kg and the effective length of the rail is 23 m. The trolley is connected with the hammer by a steel cable. Lifting or dropping hammer in the steel frame tower leads to the horizontal movement of the trolley along the rail. During testing, the hammer is raised automatically by an automatic control system, and then the trolley is dragged by the dropping hammer. When the trolley is accelerated to the designed velocity near the specimen, the cable is unhooked from the trolley, and then the trolley hits the specimen at a certain speed. The speed of trolley is related to the mass and lifting height of drop hammer. The mass of drop hammer can be varied from 200 kg to 1200 kg by the change of steel weights. The maximum lifting height of the drop hammer is 20 m. The trolley has a maximum impact velocity of 8 m/s, and the applied impact energy can be varied from 1000 J to 230,000 J. In this paper, the authors use three different impact velocities with small increment (i.e. 4 m/s, 5.5 m/s and 7 m/s) on three new specimens, respectively. The maximum applied

Table 1
Test results.

Specimen	Peak load of impact P_i (kN)	Duration (ms)	Maximum deformation (mm)	Residual deformation (mm)	Maximum acceleration (m/s^2)	Energy absorption (J)
C7–I	554.3	24.4	77.0	27.0	3477	11,135
C7-II	781.4	26.0	108.4	60.5	8243	19,197
C7-III	1022.0	29.0	143.4	97.3	14,388	28,171
C10-III	1079.9	20.9	120.6	86.0	14,788	30,177
D7-I	630.2	11.9	48.2	17.0	6112	12,565
D7-II	841.1	16.2	59.3	38.1	12,040	23,016
D7-III	1101.8	16.1	79.8	54.0	16,698	32,113
D10-III	1243.0	14.4	68.4	46.7	17,076	34,713

Note: In the first column, the first letters C and D mean CFFTs and concrete filled FRP-steel DSTCs, respectively, the numbers 7 and 10 mean the thicknesses of GFRP tubes are 7 and 10 mm, respectively, and the last numbers I, II and III mean the applied impact velocities are 4.0 m/s, 5.5 m/s and 7.0 m/s, respectively.

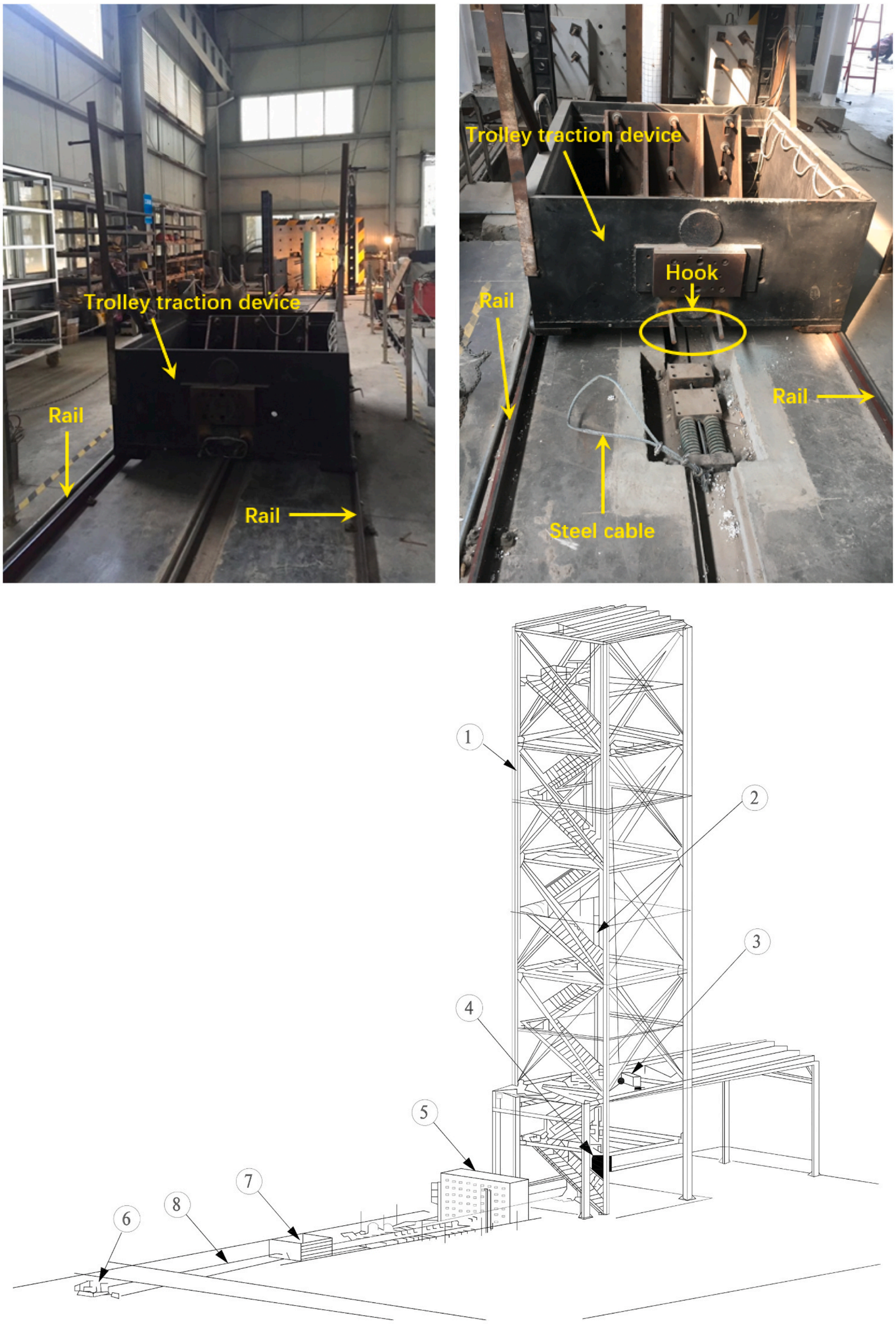

Note: 1. Steel frame tower, 2. Steel guide, 3. Gripping/releasing device, 4. Drop hammer, 5. Reaction wall, 6. Trolley traction device, 7. Trolley, 8. Rail

Fig. 2. Impact test system.

impact energy is determined by an estimated failure load for CFFT specimens which is based on the approach proposed by GangaRao and Skidmore [25]. After the impactor hitting the specimen, the trolley is immediately separated from the test specimen. The impact load was applied at 500 mm from the abutment.

The time histories of the impact force are recorded by a piezoelectric sensor mounted between the impactor and the trolley. A Linear Variable Displacement Transducer (LVDT) is used to continuously record the lateral displacement data of loading position. An acceleration transducer is mounted on each specimen to check the force history. The test setup and measurement systems are shown in Fig. 3. In addition, a high speed video camera NEX-FS700RH produced by Sony Corporation is used to record the impact process at a speed of 400 frames per second.

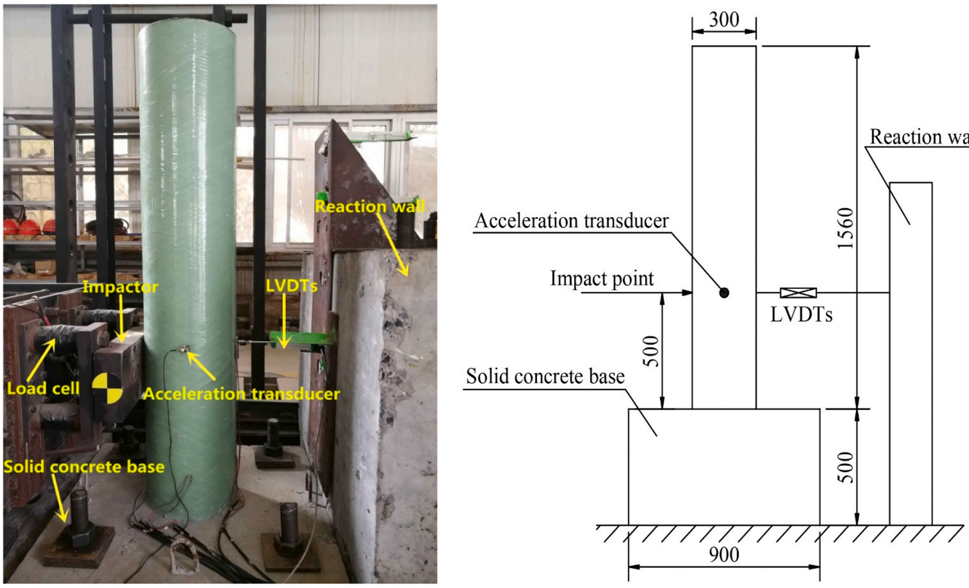

Fig. 3. Test set-up (unit: mm).

3. Results and discussion

3.1. Damage mode

The impact damages were located at the impact point and the fixed end of all the test specimens, as shown in Fig. 4. The damage at the loading point of CFFTs under the applied impact energy of 61.9 kJ (velocity = 4 m/s) was insignificant, while the increase of applied impact energy resulted in extension of the damage at the loading point. Meanwhile, concrete spalling occurred on the abutment near the fixed end of the GFRP tubes for CFFTs under the applied impact energy of 61.9 kJ. Typical failure of the CFFTs under the applied impact energies of 85.2 kJ and 108 kJ was dominated by fiber rupture in the hoop direction at the fixed end of the GFRP tubes.

Under the same applied impact energy, the damage at the loading point of concrete filled FRP-steel DSTCs was more severe than that of CFFTs, which indicated that concrete filled FRP-steel DSTCs had smaller local stiffness than CFFTs. However, the damage area at the fixed end of the concrete filled FRP-steel DSTCs was smaller than that of CFFTs.

Figs. 5 and 6 show the typical impact failure process (i.e. C7-II and D7-II) recorded by the high-speed video camera. C7-II experienced a significant lateral deformation when it collided with the trolley. Then, with the increase of lateral deformation, the contact area between C7-II and the impactor decreased, and the contact point of the column moved downwards, which resulted in the second impact. Heavy damage due to the impact resulted in high damping, thus causes a permanent deformation in C7-II. However, the lateral deformation of D7-II was much smaller than that of C7-II. After separating the impactor from the column, reciprocating vibration occurred in D7-II around the abutment.

3.2. Impact force history

The impact force-time history curves of CFFTs and concrete filled FRP-steel DSTCs are illustrated in Fig. 7. At the very beginning of impact, the impact force of the CFFTs increased sharply to a peak value. Then, the impactor and the specimens moved forward together, which resulted in a plateau of the impact force. With the increasing of global bending deformation of the specimens, the contact area between the impactor and specimen decreased and the contact point moved downward along the specimen, resulting in fluctuations of the impact force with time.

It indicated that the thickness of GFRP tubes had insignificant effect on the peak impact force. The confinement provided by GFRP tube can improve the shear and global impact behaviors of concrete. The contribution of GFRP tube also depends on the impact energy. If the impact energy is very large, the importance of FRP tube will become more significant. The specimen with thicker GFRP wall had higher local stiffness and damping, leading to the decrease in duration (The duration is the time required for the acceleration of the impact force to rise from zero to the peak value, and then decay to zero). When the impact velocity increased from 4 m/s to 7 m/s, the peak impact forces increased by 75%~84% for CFFTs and concrete filled FRP-steel DSTCs respectively, while the duration was less changed.

In the case of the same applied impact energy, the $P_{\max}$ of concrete filled FRP-steel DSTC specimens was 8–15% higher than that of CFFT specimens, while the duration of concrete filled FRP-steel DSTC specimens was around 30–50% shorter than that of CFFT specimens. The peak impact force is related to the initial local stiffness and bending stiffness of the test specimens, as well as the applied impact energy. Higher initial local stiffness and bending stiffness lead to higher peak impact force. Although the local stiffness of concrete filled FRP-steel DSTCs is smaller than that of CFFTs with the same thickness of GFRP tube, the intact concrete filled FRP-steel DSTCs have a higher bending stiffness than the intact CFFTs (when the thickness of GFRP tube is 7 mm, the bending stiffnesses of the specimens of concrete filled FRP-steel DSTC and CFFT are 12.2 MNm^2 and 12.1 $\mathrm{MN\,m}^2$, respectively), resulting in higher peak impact force in concrete filled FRP-steel DSTCs.

3.3. Displacement history

The displacement histories at impact loading location are measured, as shown in Fig. 8. All specimens showed an increased displacement as the load impacted specimens, and then displacements decreased and fluctuated at the residual deflections. The residual deformations of these two kinds of specimens were 35–70% of the maximum deformation. As applied big impact energy caused deep damage, it resulted in large residual deformations. The maximum displacement depends on the value of applied impact energy, duration and stiffness of the test specimens. Under the same applied impact energy, a longer duration resulted in the maximum displacement. However, the thickness of GFRP tubes had insignificant effect on the maximum displacement when the applied impact energy was in the range of 61.9 kJ–108 kJ. Increasing the GFRP thickness from 7 mm to 10 mm merely led to the reduction of 15% in the maximum displacement for both CFFT and concrete filled FRP-steel

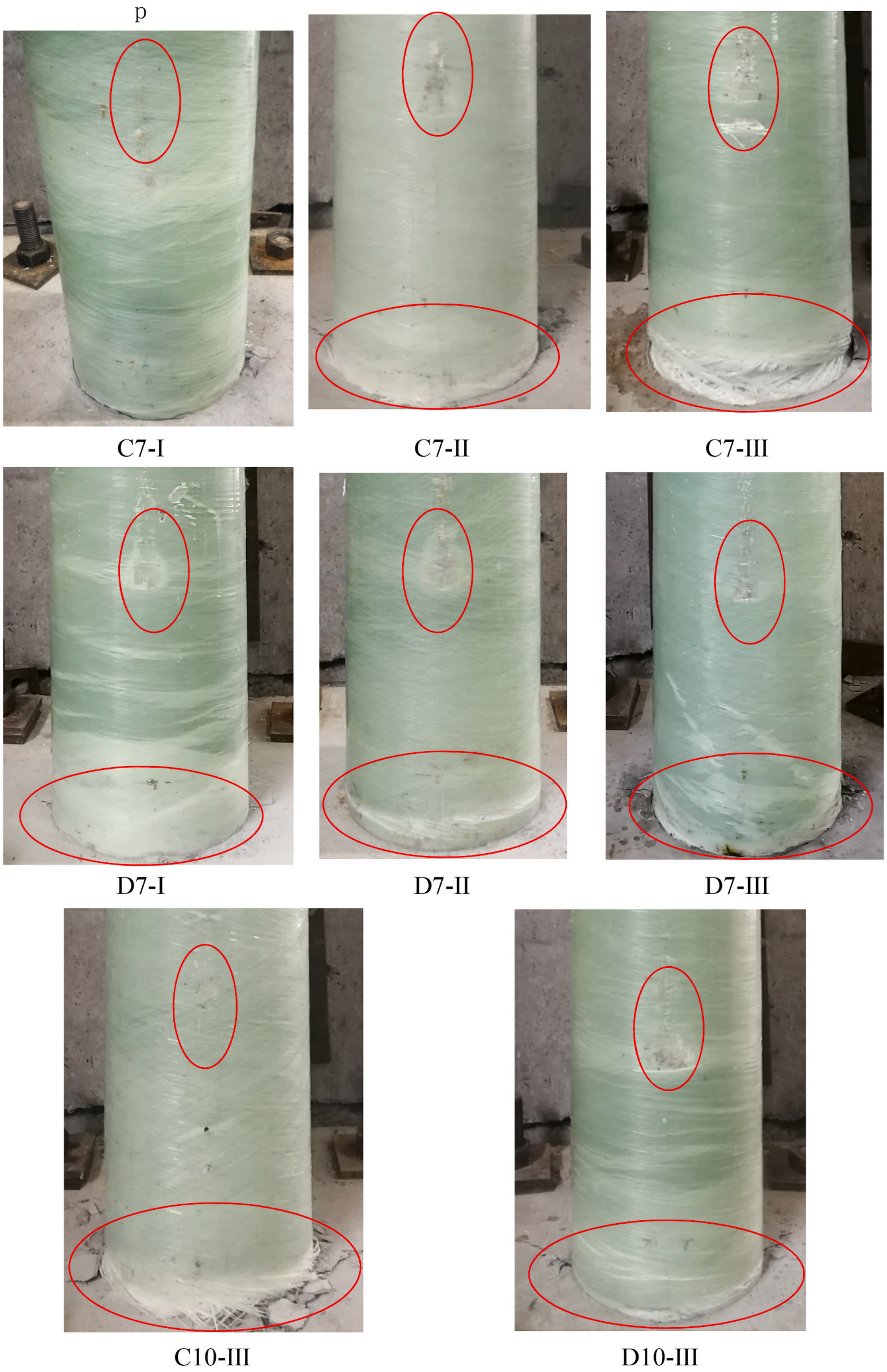

C7-I C7-II C7-III

D7-I D7-II D7-III

C10-III D10-III

Fig. 4. Impact damages.

DSTC specimens. In addition, the maximum displacement of concrete filled FRP-steel DSTC specimens was 40% smaller than that of CFFT specimens under the same applied impact energy.

3.4. Acceleration history

Fig. 9 shows the acceleration and deceleration histories of the tested specimens. Increasing the applied impact energy resulted in dramatic enhancement of the peak acceleration for both CFFT and concrete filled FRP-steel DSTC specimens, while the thickness of the GFRP had insignificant influence on the peak acceleration. In the case of the same applied impact energy, the peak acceleration of concrete filled FRP-steel DSTC specimens was 15–76% larger than that of CFFTs. It indicated that the peak force of the specimens had a trend similar to the peak acceleration (Figs. 7 and 9).

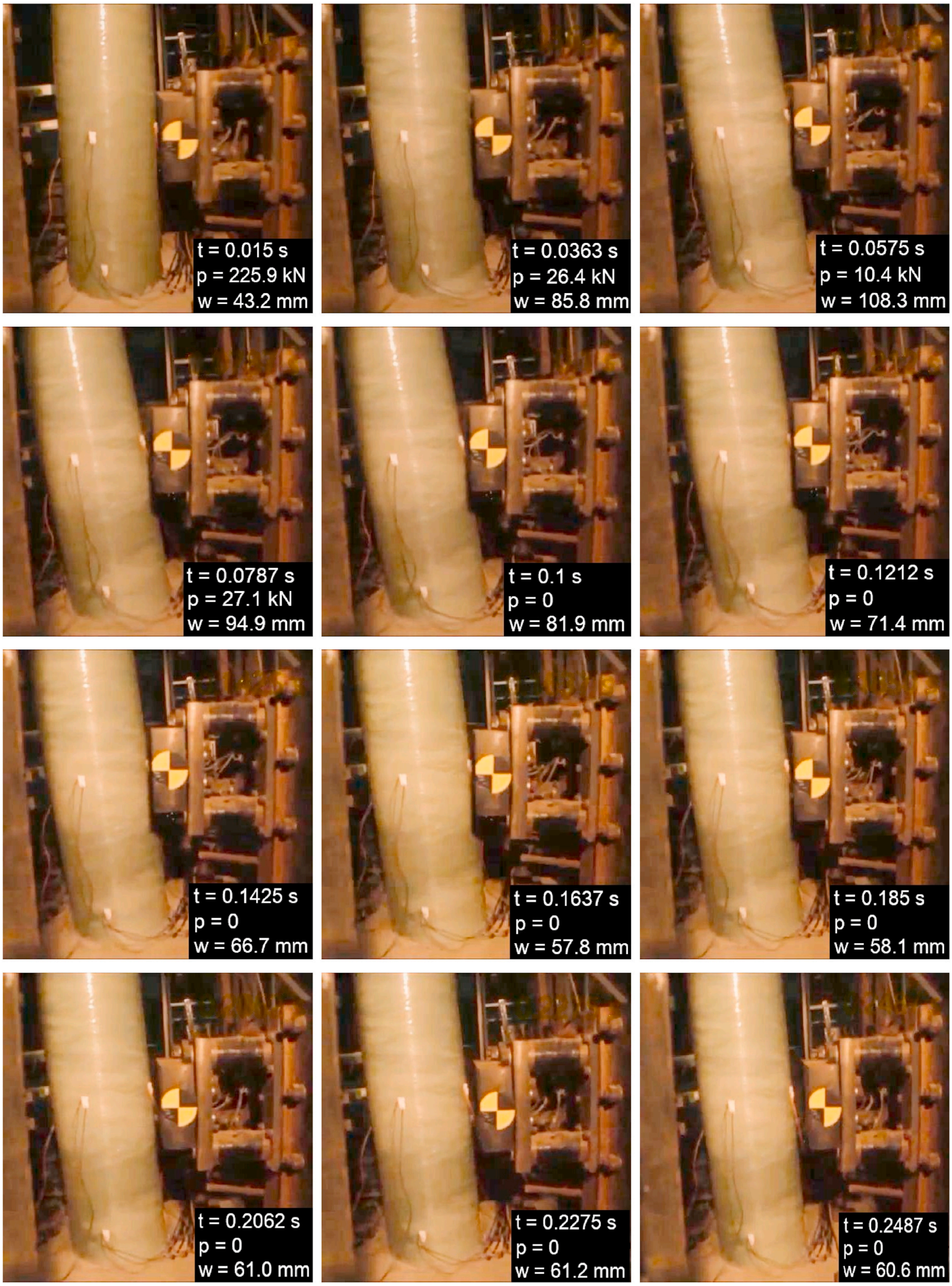

Fig. 5. Typical impact failure process (i.e. C7-II).

3.5. *Impact energy*

The capacity of energy absorption can be obtained from the relationship between the applied impact load and displacement,

$$U = \int P(w)dw \tag{1}$$

where P is applied impact load and w is displacement history at load point.

Fig. 6. Typical impact failure process (i.e. D7-II).

Table 1 lists energy absorption of tested specimens. Increasing the impact velocity from 4 m/s to 5.5 m/s and 7 m/s resulted in the enhancement of energy absorption for both CFFT and concrete filled FRP-steel DSTC specimens by ~80% and ~150%, respectively. However, the thickness of GFRP tubes had insignificant influence on the energy absorption. Under the same impact velocity, the energy absorption of concrete filled FRP-steel DSTCs was 13%~20% higher than that of CFFTs.

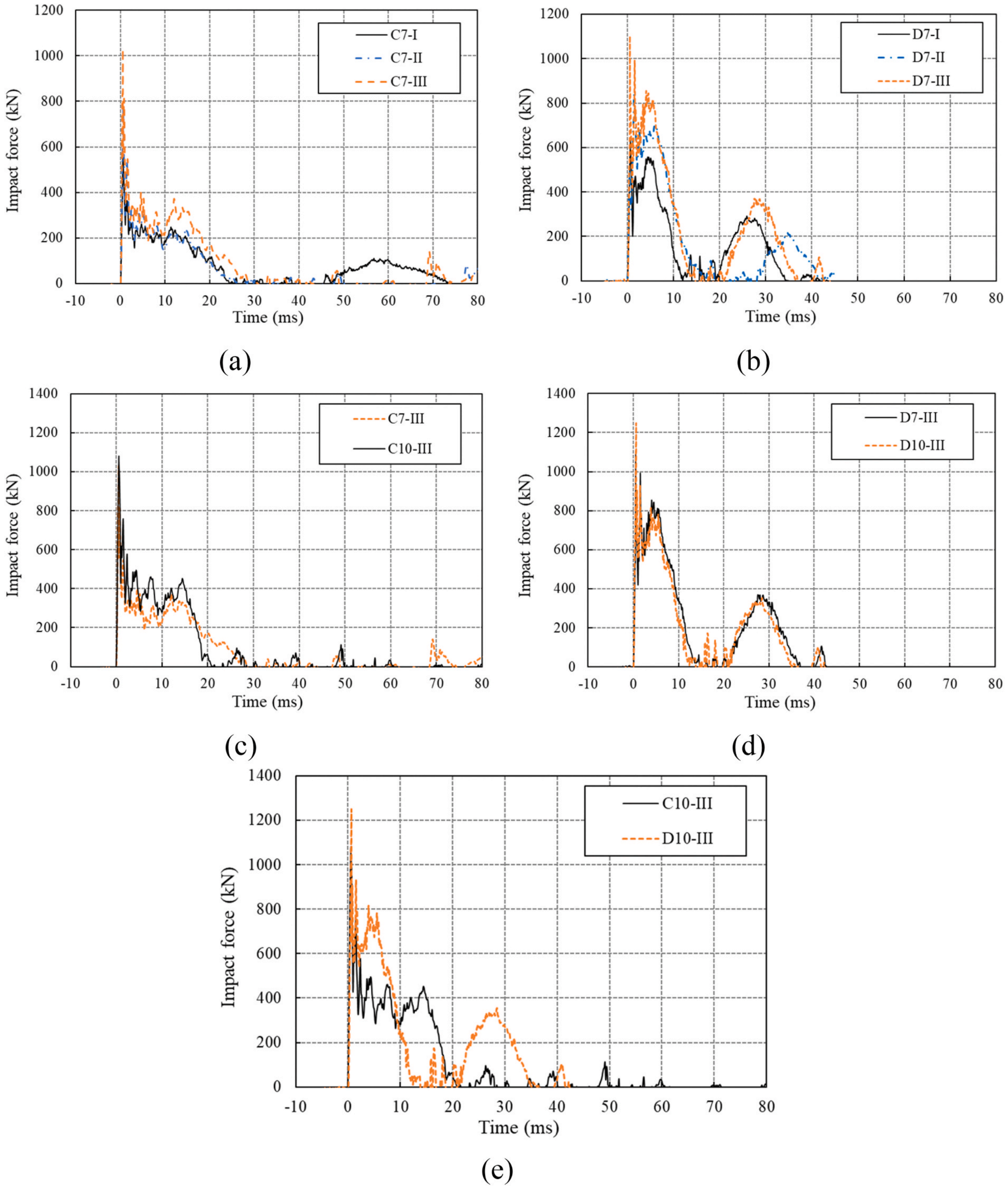

(a)

(b)

(c)

(d)

(e)

Fig. 7. Impact force-time histories.

4. Finite element simulation

In this section, a three-dimension FE model was developed using ANSYS/LS-DYNA to simulate the test specimens. Then, the verified FE model was used to analyze influences of axial loads, impact loading location, hollow ratio and normal FRP and steel ratios on the responses for both CFFTs and concrete filled FRP-steel DSTCs specimens.

4.1. Material models

Continuous surface cap model (MAT 159) was applied to describe the behavior of concrete core under impact, which included several constitutive equations to consider the strain rate effect and hydrostatic pressure on the yield stress [26]. This model is developed to simulate concrete-like materials used in fender systems at roadside subjecting collision loads induced by motor vehicles. It has been successfully used to capture the characteristic of reinforced concrete beams [27], ultra-high performance fiber reinforced beams [28] and concrete-encased concrete-filled steel tubes [29] under low–velocity impacts. Only three inputs (the unconfined compressive strength, aggregate size and the units used in the finite element model) are required in this model to generate default parameters for concrete with

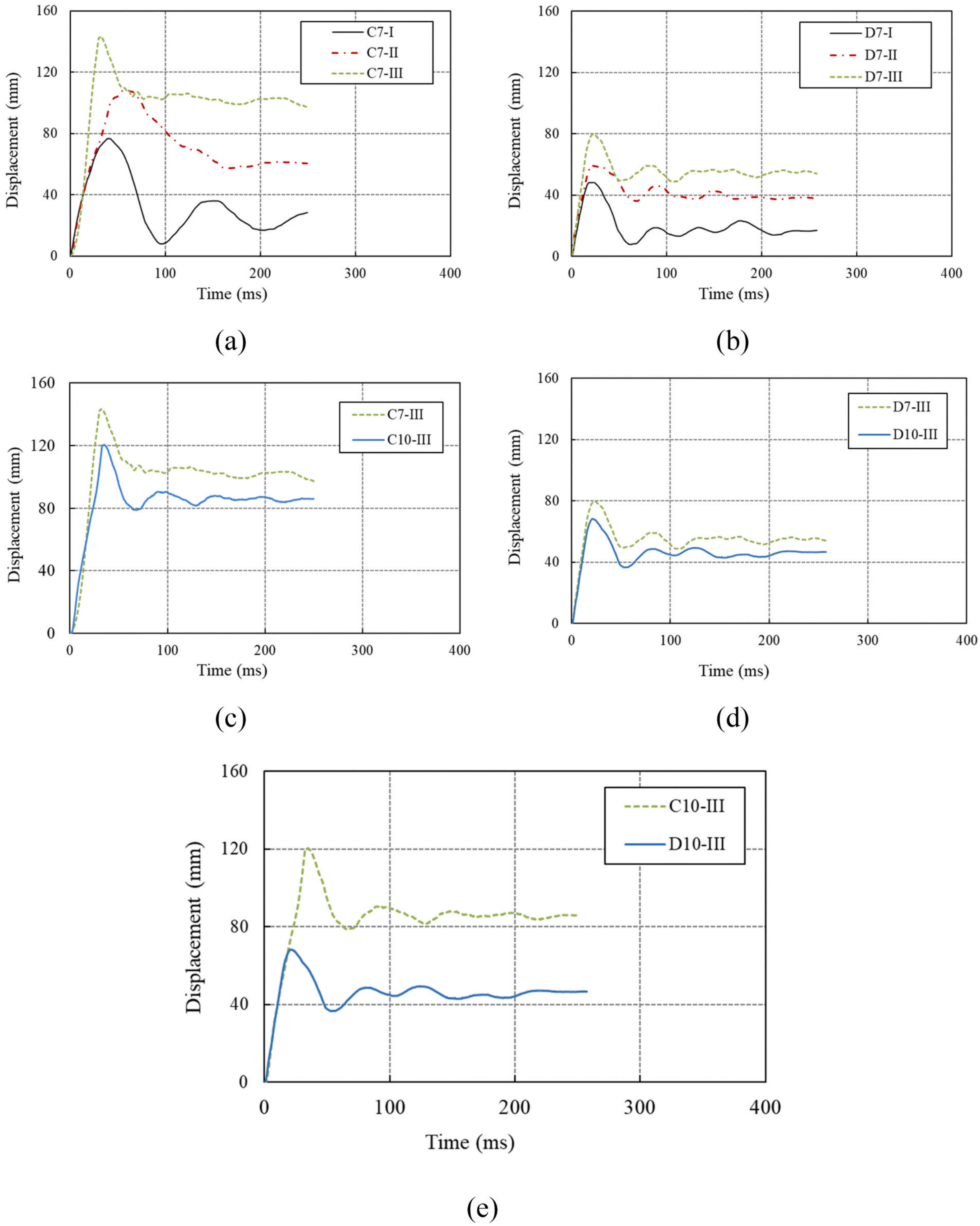

Fig. 8. Displacement histories.

the unconfined compressive strength in the range of 20–58 MPa and the aggregate sizes from 8–32 mm [27]. The input parameters for the concrete are listed in Table 2.

FRP materials were simulated by "055-enhanced composite damage" model which approximated a linear elastic behavior until failure. This model is one of outcomes of recent development of modeling studies thus is selected because of its relative simplicity as well as the superior performance in simulation of collision [30]. The Tsai-Wu criterion was used to predict the failure of GFRP tubes in this investigation. The input parameters for the FRP are listed in Table 3.

The inner steel tubes were simulated by bilinear kinematic plasticity model (MAT_PLASTIC_KINEMATIC) with Von Mises yield criterion. The strain rate effect was considered to calculate the dynamic increase factor for the inner steel tube (DIF_S), as given by [31,32].

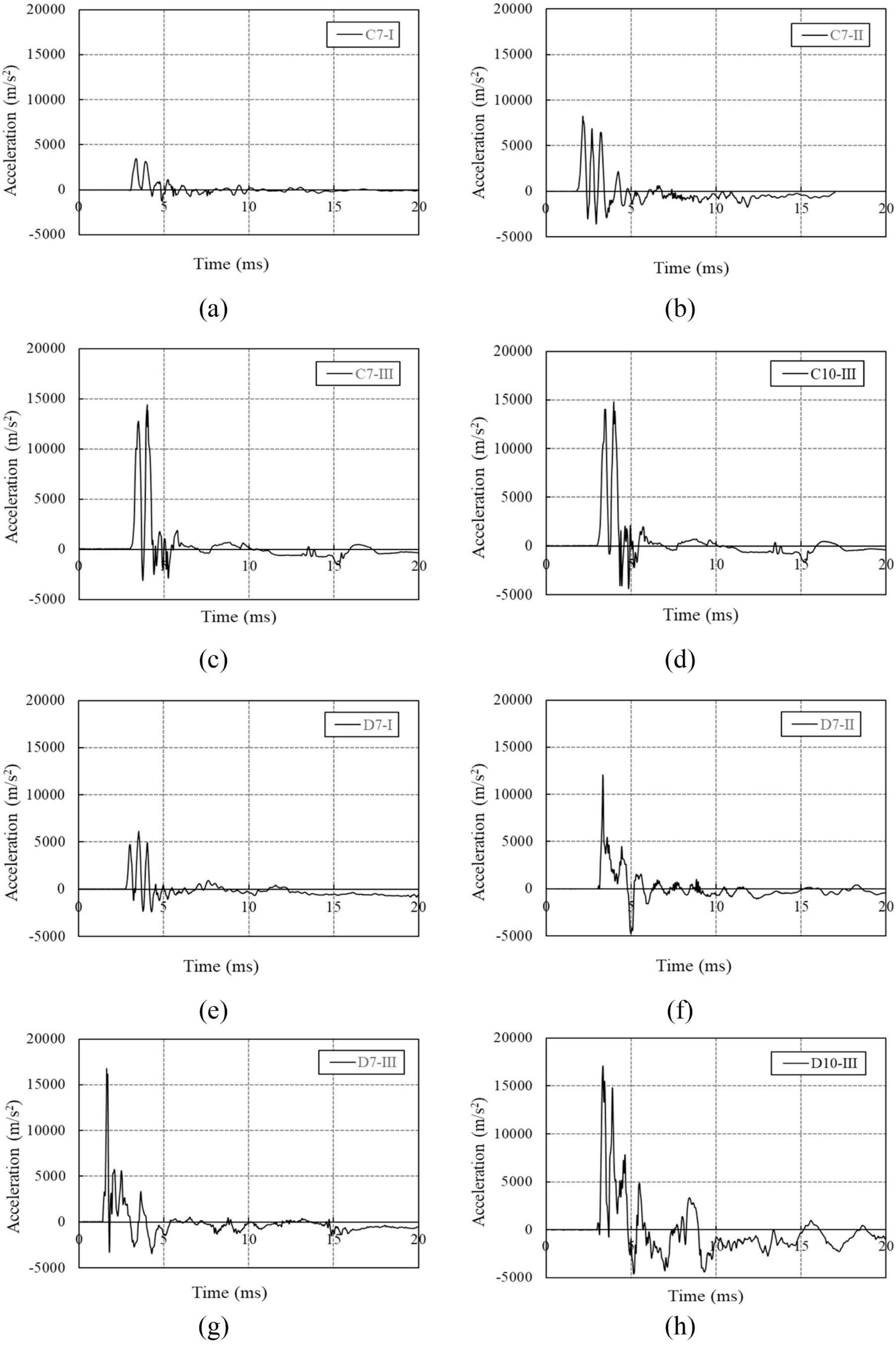

(a) (b) (c) (d) (e) (f) (g) (h)

Fig. 9. Acceleration histories.

Table 2
Mechanical properties of concrete.

Density (kg/m^3)	Compressive strength (MPa)	Young's modulus (GPa)	Poission's ratio	Maximum aggregate size (mm)	Initial damage
2500	28	28	0.2	20	0

$$DIF_s = 1 + \left(\frac{\dot{\varepsilon}}{C}\right)^{1/P} \tag{2}$$

where $\dot{\varepsilon}$ is the strain rate of the steel tube, P and C are parameters related to strain harden effect and material types. In this investigation, P and C are taken as 5 and 40 s^{-1}, respectively. The stress-strain curve of steel in elastic-plastic phase is simplified as a bi-linear relationship, contains formulations incorporating isotropic and kinetic hardening. The yield stress and failure strain of the steel tube are 278 MPa and 0.2, respectively. The input parameters for the steel are listed in Table 4.

The impactor was made of high strength steel, so it was simulated by isotropic hypo-elastic material model (Mat_Rigid). The mass, modulus and Possion's ratio were set to be 1580 kg, 210 GPa and 0.3, respectively.

4.2. FE model construction

The concrete and impactor were modeled by Solid 164 3-D solid element, while GFRP and steel tubes were modeled by Shell 163 element. One end of the specimens was assumed to be fixed, and the other end was free. The impactor could only move in horizontal direction by constraint definition. The initial velocity of the impactor was imposed by the command *INITIAL_VELOCITY_RIGID_BODY.

Sensitivity analysis was carried out for different mesh sizes (i.e. 10 mm, 15 mm and 20 mm). The impact responses of test specimens can be captured properly with mesh size from 10 mm to 20 mm (Fig. 10). The element size is taken as 10 mm because further decrease in mesh size almost generated the same results while the computational time increases considerably. Surface-to-surface contact elements were used to simulate the interface between the impactor and GFRP, the concrete and GFRP tube, and even the concrete and steel tube. Master and slave formulations were applied to define the form of contact between the different surfaces (i.e. steel impactor was the master surface and GFRP was the slave surface for impactor/GFRP surface). This type of contact considers slip and separation. Hence, slip/debonding is displayed if either occurs between the concrete surface and GFRP surface, and between the concrete surface and steel surface [17]. The friction coefficient was taken as 0.22 for the contact surface of the outer GFRP tube and concrete core, 0.25 for the contact surface of steel impactor and outer GFRP tube, as well as the inner steel tube and concrete, respectively [33].

4.3. Comparison of numerical and experimental results

The damage modes of simulated specimens C7-III and D7-III are shown in Fig. 11. For specimen C7-III, the maximum longitudinal compressive stress occurred at the loading point, and the maximum longitudinal tensile stress occurred at the fixed end, resulting in resin crushing at the loading point and fiber rupture in the hoop direction at the fixed end. The maximum lateral tensile stress of C7-III occurred on both sides of the loading point, while the lateral compressive stress was much lower than the longitudinal compressive stress. For specimen D7-III, the maximum longitudinal tensile stress occurred simultaneously at the loading area and the fixed end, resulting in local buckling and crushing at the loading area. The distribution of lateral stress of D7-III was similar with that of C7-III.

The numerical and experimental impact force-time histories for CFFT and concrete filled FRP-steel DSTC specimens are shown in Fig. 12. The numerical curves in Fig. 12 shows that the model offers reasonable trend with the test data, i.e., FE analyses is capable of capturing the overall shapes of the tested impact force-time histories. Table 5 reveals that the numerical peak impact forces are in good agreement with the experimental values.

4.4. Parametric studies

4.4.1. Influence of axial loads

Composite columns used as bridge piers are designed to carry the vertical load from superstructures. Due to the limit of impact test system, our test specimens are not applied with the axial loads. Hence, the validation of FE models for specimens subjected to combined axial loading and lateral impact were conducted in two step process. In the

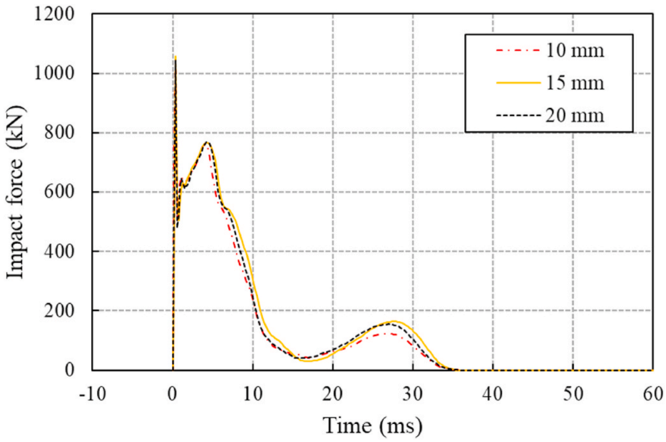

Fig. 10. Simulated impact force histories for specimen D7-III under different mesh sizes.

Table 3
Mechanical properties of GFRP tube.

Density (kg/m^3)	Axial direction					Hoop direction		
	Compressive strength (MPa)	Compressive modulus (GPa)	Tensile strength (MPa)	Tensile modulus (GPa)	Poisson's ratio	Tensile strength (MPa)	Tensile modulus (GPa)	Poisson's ratio
1800	161	12	120	12.5	0.3	250	22	0.22

Table 4
Mechanical properties of steel tube.

Density (kg/m^3)	Young's modulus (GPa)	Poission's ratio	Yield stress (MPa)	Tangent modulus (GPa)	Strain rate parameter C (s^{-1})	Strain rate parameter P	Failure strain
7850	201	0.3	278	6.1	40	5	0.2

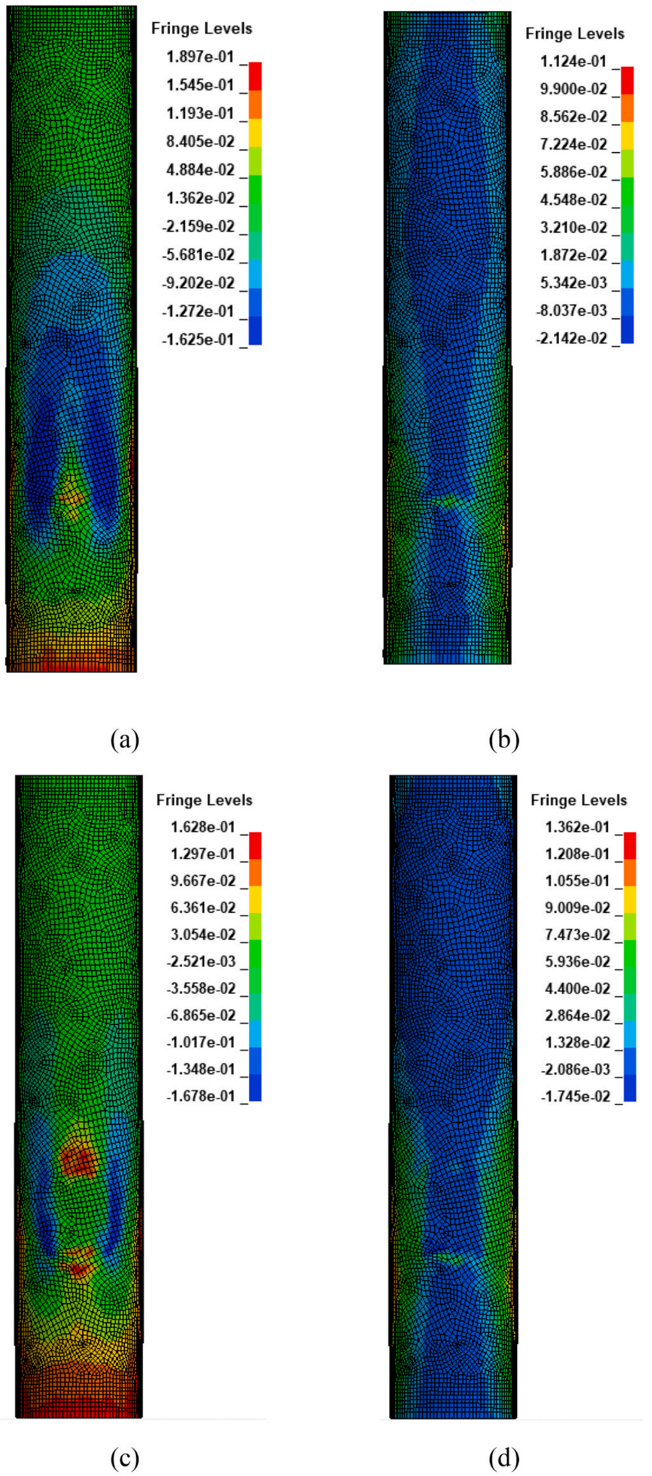

(a) (b)

(c) (d)

Fig. 11. Stress contour at failure (unit: GPa, tensile stress as positive and compressive stress as negative): (a) C7-III (longitudinal stress); (b) C7-III (lateral stress); (c) D7-III (longitudinal stress); (d) D7-III (lateral stress).

first step, the impact simulation process was validated by developing FE model of test specimens without axial loads and validating the numerical results with impact tests. The comparison results have been mentioned in section 4.3. Later in the second step, concrete filled steel tubular (CFST) column and concrete-filled double-skin tube (CFDST) column subjected to combined axial loading and lateral impact were modeled and validated with the test results conducted by Wang et al. [34] and Aghdamy et al. [22], respectively. Axial force is applied as a combination of forces on the FRP and concrete areas separately for CFFT specimens, or as a combination of forces on the FRP, concrete and steel areas separately for concrete filled FRP-steel DSTC specimens by assuming uniform strain distribution.

The results obtained from the FE analysis are compared with the experiments of Wang et al. [34] and Aghdamy et al. [22]. Failure modes of FE analysis models were similar with the tested columns (Fig. 13). Moreover, good matching between impact force histories of these two types of column was noticed (Fig. 14).

The impact simulation of CFFT and concrete filled FRP-steel DSTC columns was performed by adopting the CFST and CFDST column impact simulation process to ensure reliable numerical analysis of the effect of axial load.

Both axial load and impact load were applied on the specimens at the same time in FE models. The axial compression ratio (ACR) of CFFTs is defined as

$$\lambda = \frac{N}{f_F A_F + f_c^{'} A_c} \tag{3}$$

where N is the axial load applied on the columns, f_F and A_F are the axial compression strength and cross-sectional area of FRP tubes, respectively, and $f_c^{'}$ and A_c are the confined strength of concrete and cross-sectional area of FRP tubes, respectively. The confined strength of concrete in CFFTs can be obtained from Lam and Teng's work [5].

The axial compression ratio of concrete filled FRP-steel DSTCs is defined as

$$\lambda^{'} = \frac{N}{f_F A_F + f_c^{'} A_c + f_s A_s} \tag{4}$$

where f_s and A_s are the confined strength of concrete and cross-sectional area of FRP tubes, respectively. The confined strength of concrete in concrete filled FRP-steel DSTCs can be obtained from Teng et al. [35].

According to GB 50010–2010 [36], the maximum value of ACR of concrete columns is less than 0.65. The impact force histories of C7-II and D7-II with ACR varied from 0, 0.2 to 0.6 were calculated, respectively. It is shown in Fig. 15 that the ACR has insignificant influence on the impact force history of C7-II. However, the peak impact force of D7-II decreased by 33% accompanied by the decrease in the stiffness when the ACRs increased from 0 to 0.6. In the case of ACR = 0.6, the impact energy applied on D7-II was dissipated mostly in irreversible plastic deformation.

4.4.2. *Influence of impact loading location*

Three different distances between the impact loading location and abutment (i.e., $l_0 = 0.5$, 1.0, and 1.5 m) were tried on C7-II and D7-II specimens, respectively. Each specimen was impacted only once. Fig. 16 shows the impact force histories for both C7-II and D7-II specimens under different impact loading points. When l_0 was less than 1.0 m, it had insignificant influence on the impact force histories of C7-II. Further increasing l_0 from 1.0 m to 1.5 m resulted in 25% decrease of peak impact force of C7-II. On the other hand, the increases of l_0 from 0.5 m to 1.5 m resulted in a gradual reduction of peak impact force of D7-II.

4.4.3. *Influence of hollow ratio*

Hollow ratio ϕ is defined as the ratio between the inner diameter and the outer diameter of the annular concrete section [37]. The hollow ratio ϕ is an important parameter affecting the mechanical behavior of concrete filled FRP-steel DSTCs. The hollow ratio ϕ of the tested concrete filled FRP-steel DSTC specimens is 0.47. In the case of the same outer GFRP tube, three different hollow ratios (i.e., $\phi = 0.3$, 0.47, and 0.6) were tried on concrete filled FRP-steel DSTCs. Fig. 17 shows the impact force histories for concrete filled FRP-steel DSTC members with different ϕ under the applied impact energy of 85.2 kJ. The concrete filled FRP-steel DSTC member with hollow ratio of 0.3 had similar impact

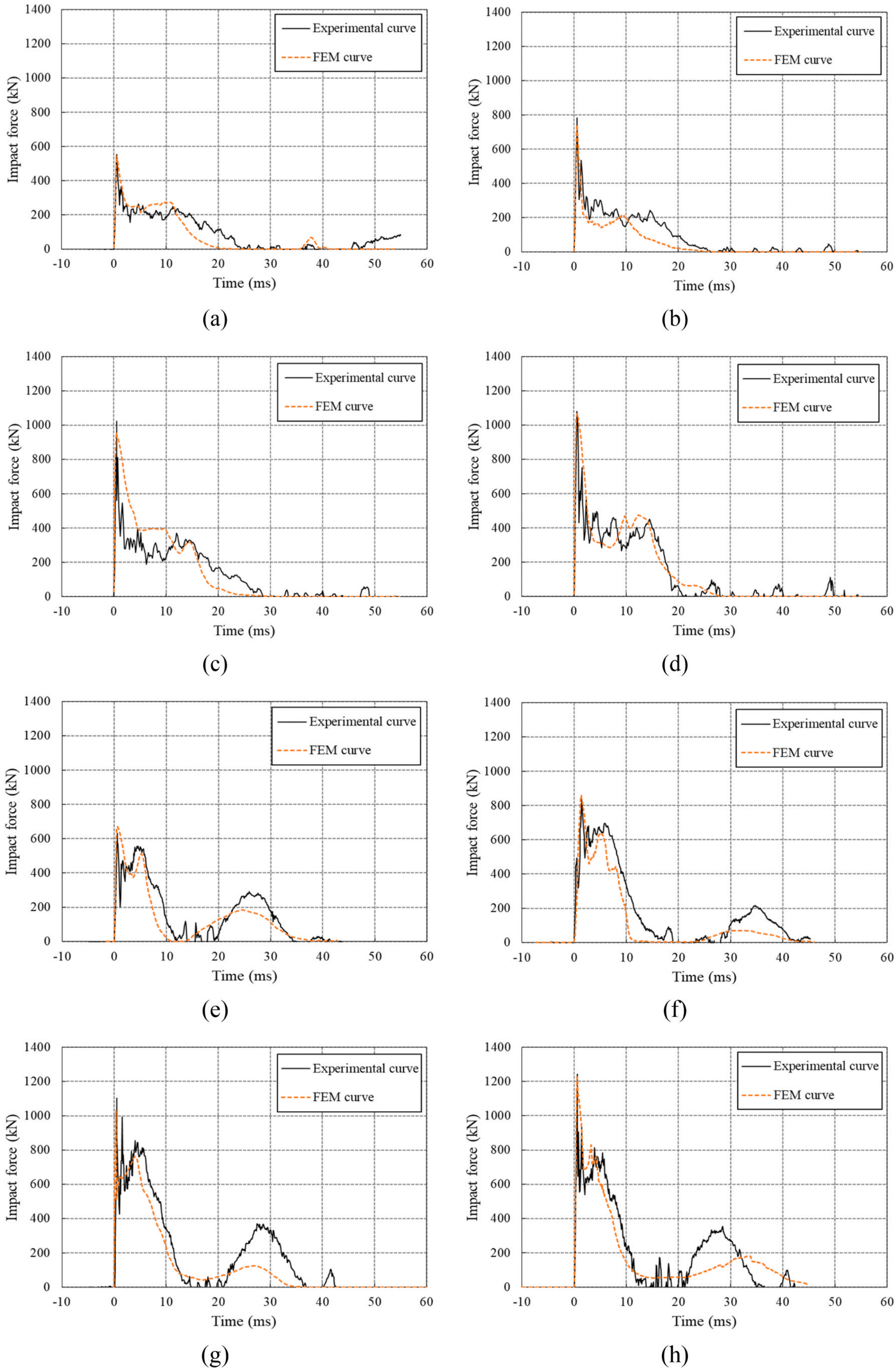

Fig. 12. Comparison of numerical and experimental impact force histories for (a) C7–I; (b) C7-II; (c) C7-III; (d) C10-III; (e) D7-I; (f) D7-II; (g) D7-III and (h) D10-III.

Table 5
Comparison of peak impact forces between numerical and experimental results.

Specimen	Tested peak impact force P_1 (kN)	Numerical peak impact force P_2 (kN)	$\delta = \frac{P_2 - P_1}{P_1} \times$ 100%
C7–I	554.3	545.1	−1.7
C7-II	781.4	742.3	−5.0
C7-III	1022.0	955.6	−6.5
C10-III	1079.9	1067.0	−1.2
D7-I	630.2	670.1	6.3
D7-II	841.1	858.7	2.1
D7-III	1101.8	1033.7	−6.2
D10-III	1243.0	1225.2	−1.4

force history with that of member with hollow ratio of 0.47. Increasing ϕ from 0.3 to 0.6 resulted in 29% decrease of impact force and 9% increase of duration.

4.4.4. Influence of nominal FRP and steel ratios

The normal FRP ratio α_f is defined as the ratio between the cross-sectional areas of FRP tube and concrete [38], and the normal steel ratio α_s is defined as the ratio between the cross-sectional areas of steel tube and concrete.

Four different α_f (i.e., 0.0955, 0.1378, 0.1808 and 0.2312) were tried on CFFTs, corresponding to the thickness of GFRP outer tube of 7 mm, 10 mm, 13 mm and 16.4 mm. It can be seen from Fig. 18(a) that with the increment of α_f, the impact force increases gradually and the duration decreases obviously for CFFTs under the applied impact energies of 108 kJ. Increasing α_f from 0.0955 to 0.2312 resulted in 25% increase in the peak impact force and 54% decrease in duration for CFFTs. Meanwhile, three different α_f (i.e., 0.1221, 0.1761 and 0.2312) were tried on concrete filled FRP-steel DSTCs, corresponding to the thickness of GFRP outer tube of 7 mm, 10 mm and 13 mm. As shown in Fig. 18(b), the impact force increases insignificantly and duration decreases gradually with the increment of α_f for concrete filled FRP-steel DSTCs under the applied impact energies of 108 kJ. Increasing α_f of concrete filled FRP-steel DSTCs from 0.1221 to 0.2312 resulted in 11% increase in the peak impact force and 22% decrease in duration. In the case of $\alpha_f =$ 0.2312, the concrete filled FRP-steel DSTC exhibited 8% decrease in the peak impact force, and 17% increase in the duration compared with CFFT. Generally, α_f has a more significant influence on the duration than on the impact peak force for CFFTs and concrete filled FRP-steel DSTCs. Concrete filled FRP-steel DSTCs have lower peak impact force and longer duration than CFFTs with the same α_f, due to the thicker FRP outer tube in the former members. In addition, by increasing α_f of CFFTs

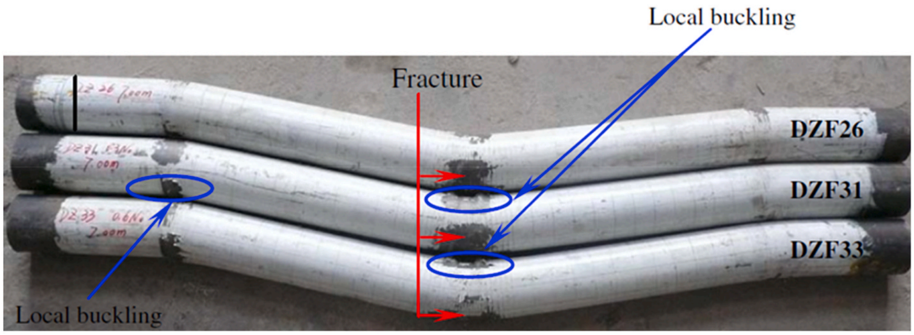

Test result of the CFST column with name of DZF31 in Ref. [34]

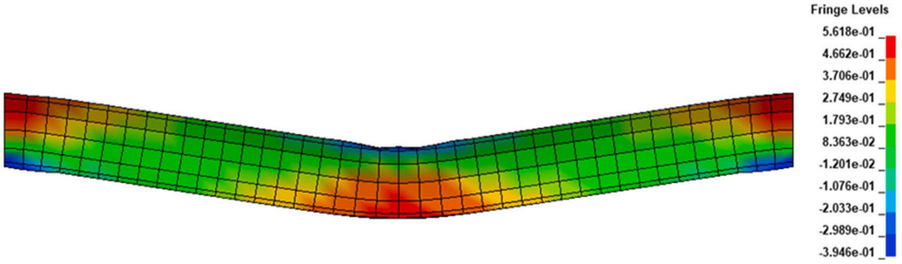

FE analysis of the CFST column with name of DZF31

Test result of the CFDST column with name of CFDST3B in Ref. [22]

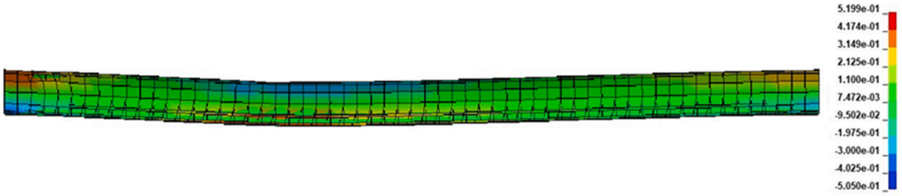

FE analysis of the CFDST column with name of CFDST3B

Fig. 13. Comparison of failure modes between test and present FE analysis (unit: GPa).

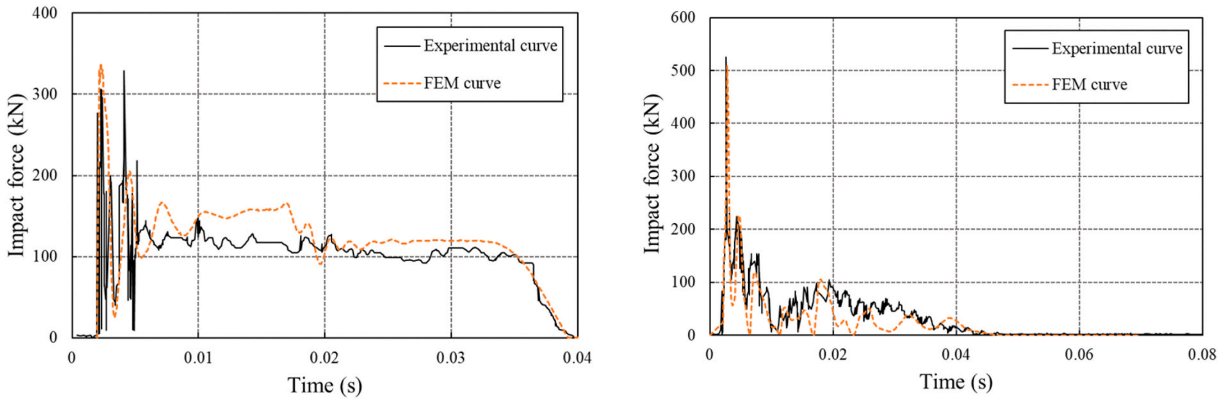

(a)

(b)

Fig. 14. Comparison of impact load histories between test and present numerical results for (a) the CFST column in Ref. [34] (the name of specimen is DZF31); (b) the CFDST column in Ref. [22] (the name of specimen is CFDST3B).

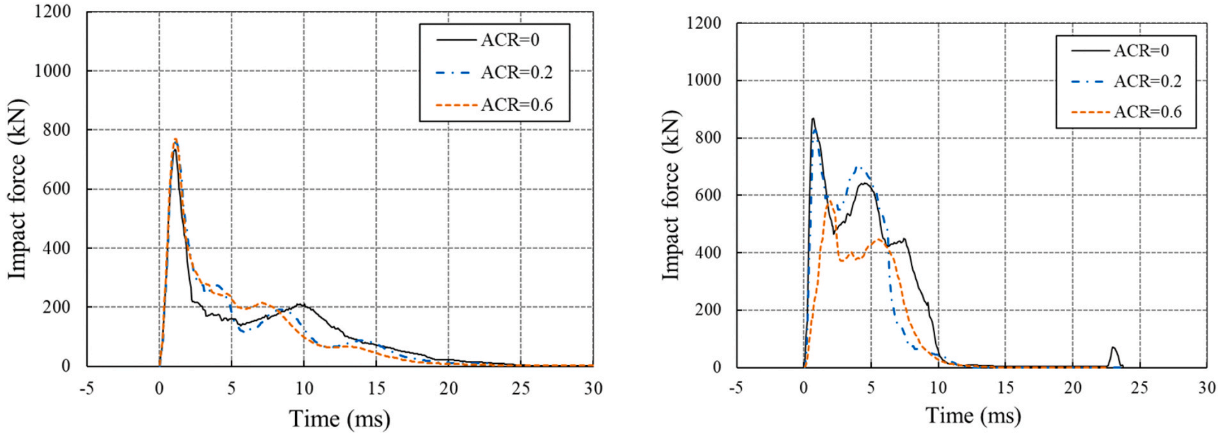

(a)

(b)

Fig. 15. Simulated impact load histories of specimens with different axial compression ratios for (a) C7-II and (b) D7-II.

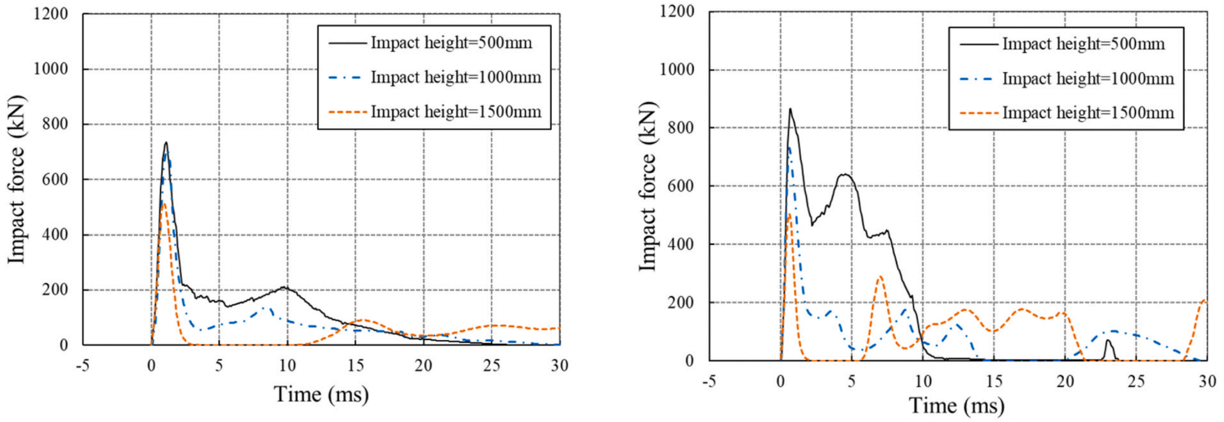

(a)

(b)

Fig. 16. Simulated impact load histories of specimens with different impact heights for (a) C7-II and (b) D7-II.

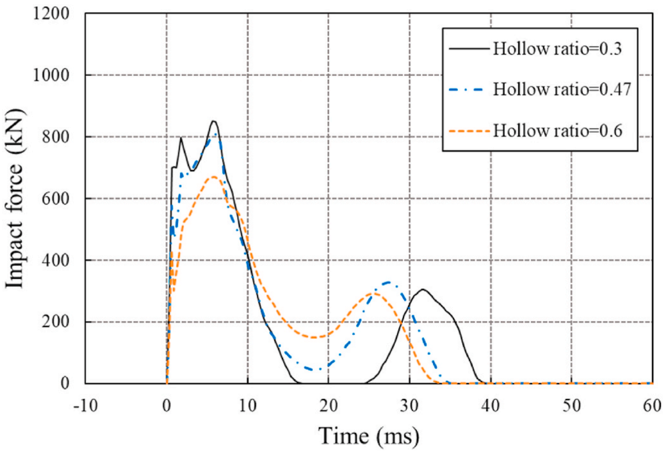

Fig. 17. Simulated impact load histories of concrete filled FRP-steel DSTC specimens with different hollow ratio.

from 0.0955 to 0.2312, the slenderness ratio λ decreased from 39.8 to 37.5. Meanwhile, by increasing α_f of concrete filled FRP-steel DSTCs from 0.1221 to 0.2312, λ decreased from 36.6 to 35.4. Varying the thickness of GFRP led to insignificant change in λ. The λ of composite columns studied in this paper are within the slenderness limit (<40) [39]. The impact responses of slender columns are not included herein.

Three different α_s (i.e., 0.0234, 0.0457 and 0.067) were tried on concrete filled FRP-steel DSTCs, corresponding to the thickness of steel inner tube of 3 mm, 6 mm and 9 mm. Increasing α_s from 0.0234 to 0.067 resulted in 16% increase in the peak impact force and 14% decrease in duration for concrete filled FRP-steel DSTCs (Fig. 19). The specimen with thicker inner steel tube had higher local stiffness, which led to the increase in the peak impact force and the decrease in the duration.

5. Analytical model of the impact responses

In the derivation of the deformation responses of a composite column under lateral impact, a test specimen was assumed to be axially inextensible and its behavior followed the Euler-Bernoulli beam theory. Then the influences of shear deformation and rotary inertia terms on the natural frequencies of the beam were considered. The boundary conditions were considered as clamp-free.

5.1. Impact theory

The differential equation for lateral displacement of a uniform cantilever beam subjected to impact is shown as [40,41].

$$m\frac{\partial^2 W(x,t)}{\partial t^2}+C\frac{\partial W(x,t)}{\partial t}+EI\frac{\partial^4 W(x,t)}{\partial x^4}=P(x,t) \tag{5}$$

where $W(x, t)$ = the lateral displacement, m = mass of the beam per unit length, C = damping intensity of the beam, E = Young's modulus of the materials, I = inertia of the cross section and $P(x, t)$ = impact load function.

$W(x, t)$ can be considered as the sum of a series of products of spatial functions of only x and time-dependent functions as

$$W(x,t)=\sum_{i=1}^{\infty}\varphi_i(x)w_i(t) \tag{6}$$

where $\varphi_i(x)$ are the eigenfunctions of a linear uniform cantilever beam and $w_i(t)$ are the generalized time-dependent coordinates.

Substituting Eq. (6) into Eq. (5), multiplying $\varphi_j(x)$ on both sides of Eq. (5) and then integrating each term of Eq. (5) over span l, we obtained [20].

$$\ddot{w}_i(t)+2\xi_i\omega_i\dot{w}_i(t)+\omega_i^2 w_i(t)=\int_0^l \frac{P(x,t)\varphi_i(x)}{m}dx \tag{7}$$

in which

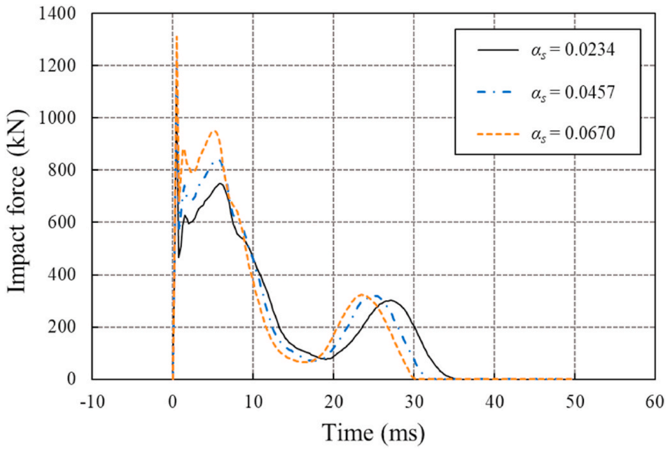

Fig. 19. Simulated impact load histories of concrete filled FRP-steel DSTCs with different α_s.
Note: 1. Steel frame tower, 2. Steel guide, 3. Gripping/releasing device, 4. Drop hammer, 5. Reaction wall, 6. Trolley traction device, 7. Trolley, 8. Rail.

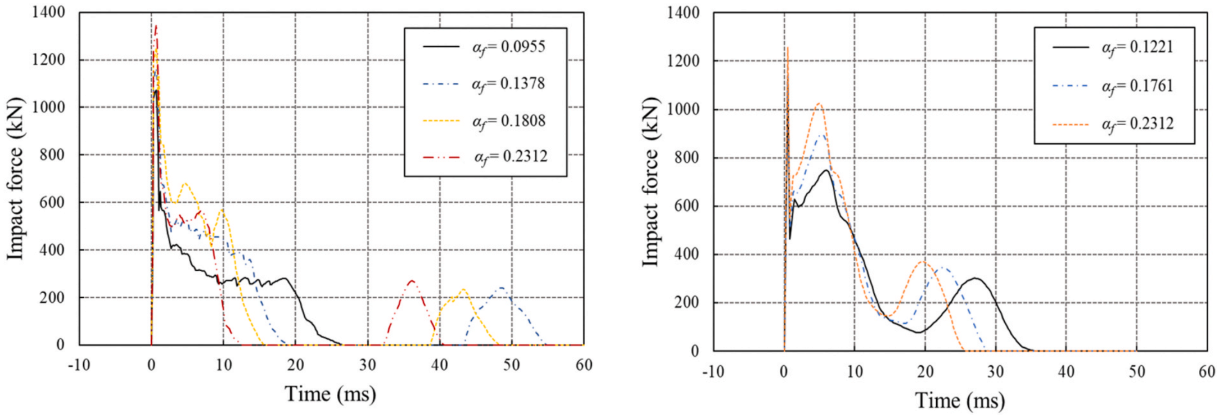

(a) CFFTs

(b) Concrete filled FRP-steel DSTCs

Fig. 18. Simulated impact load histories of specimens with different α_f for (a) CFFTs and concrete filled FRP-steel DSTCs.

$$\xi_i = \frac{c}{2m\omega_i}$$

where ω_i is the eigenvalue of a linear uniform cantilever beam.

The expression of impact force $P(x, t)$ was assumed as a dual function (Fig. 20), because the measured impact force histories exhibited a linear phase before the peak load was reached and then the impact force decreased nonlinearly. In the first phase, the impact force history was simulated by a linear function, and in the second phase, the impact force history was simulated by an exponential function. Thus, the impact function can be expressed as follows:

$$P(x,t) = \begin{cases} \dfrac{P_0}{t_1} t\delta(x-l_0) & 0 \le t \le t_1 \\ P_0 \cdot e^{-a(t-t_1)}\delta(x-l_0) & t_1 < t \end{cases} \tag{8}$$

where P_0 and t_1 are the peak value of impact force and the corresponding time, respectively. δ is the unit pulse function, l_0 is the distance between the loading point and the clamped end of the beam, and a is a factor which is determined by fitting the decrease phase with the exponential function.

The vibration equation of modal coordinates can be obtained by substituting Eq. (8) into Eq. (7).

In the case of $0 \le t \le t_1$,

$$\ddot{w}_{i1}(t) + 2\xi_i\omega_i\dot{w}_{i1}(t) + \omega_i^2 w_{i1}(t) = \frac{k_i P_0}{t_1} t \tag{9}$$

where $k_i = \frac{\varphi_i(l_0)}{m\int_0^l \varphi_i^2(x)dx}$.

The solution of w_{i1} is

$$w_{i1}(t) = \frac{k_i P_0}{t_1 {\omega_i}^3}\left[2\xi_i \cos\left(\omega_i\sqrt{1-{\xi_i}^2}\, t\right) + \frac{2{\xi_i}^2 - 1}{\sqrt{1-{\xi_i}^2}} \sin\left(\omega_i\sqrt{1-{\xi_i}^2}\, t\right)\right] e^{-\xi_i\omega_i t} - \frac{2\xi_i k_i P_0}{t_1 {\omega_i}^3} + \frac{k_i P_0}{t_1 {\omega_i}^2} t \tag{10}$$

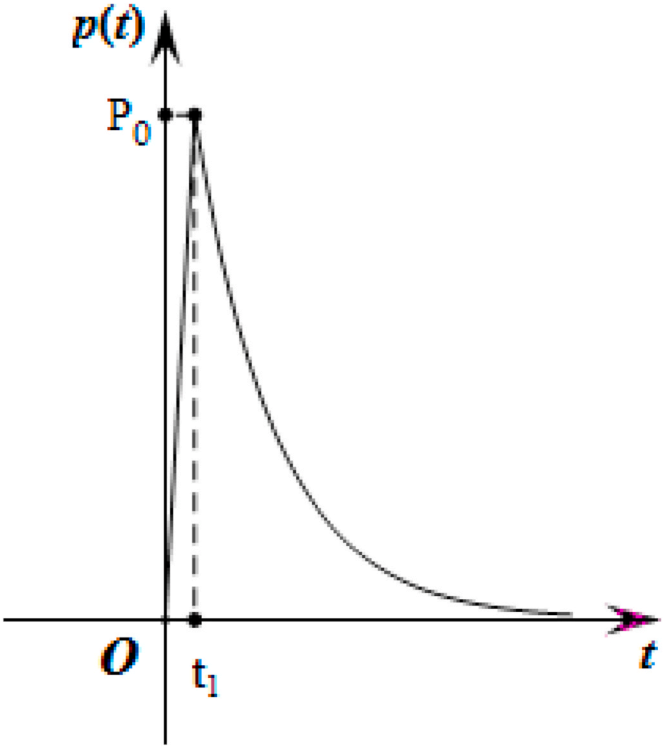

Fig. 20. Sketch of a dual function to simulate the impact load histories.

In the case of $t_1 < t$,

$$\ddot{w}_{i2}(t) + 2\xi_i\omega_i\dot{w}_{i2}(t) + \omega_i^2 w_{i2}(t) = k_i P_0 \cdot e^{-a(t-t_1)} \tag{11}$$

The solution of w_{i2} is

$$w_{i2}(t) = \left[A_i \cos\left(\omega_i\sqrt{1-{\xi_i}^2}\, t\right) + B_i \sin\left(\omega_i\sqrt{1-{\xi_i}^2}\, t\right)\right] e^{-\xi_i\omega_i t} + \frac{k_i P_0}{(a^2 - 2a\xi_i\omega_i + \omega_i^2)} e^{-a(t-t_1)} \tag{12}$$

When $t = t_1$, $w_{i1}(t_1) = w_{i2}(t_1)$, $\dot{w}_{i1}(t_1) = \dot{w}_{i2}(t_2)$. Thus A_i and B_i for a cantilever beam are obtained as follow

$$A_i = \frac{2\xi_i k_i P_0}{t_1 {\omega_i}^3} - k_i P_0 e^{\xi_i\omega_i t_1}\left(\frac{2\xi_i}{t_1{\omega_i}^3} - \frac{1}{{\omega_i}^2} + \frac{1}{a^2 - 2a\xi_i\omega_i + {\omega_i}^2}\right)\cos\left(\omega_i\sqrt{1-{\xi_i}^2} t_1\right) + \frac{k_i P_0}{\omega_i\sqrt{1-{\xi_i}^2}} e^{\xi_i\omega_i t_1}\left(\frac{2{\xi_i}^2 - 1}{t_1{\omega_i}^2} + \frac{\xi_i\omega_i - a}{a^2 - 2a\xi_i\omega_i + {\omega_i}^2} - \frac{\xi_i}{\omega_i}\right)\sin\left(\omega_i\sqrt{1-{\xi_i}^2} t_1\right) \tag{13}$$

$$B_i = \frac{k_i P_0(2{\xi_i}^2 - 1)}{t_1{\omega_i}^3\sqrt{1-{\xi_i}^2}} - k_i P_0 e^{\xi_i\omega_i t_1}\left(\frac{2\xi_i}{t_1{\omega_i}^3} - \frac{1}{{\omega_i}^2} + \frac{1}{a^2 - 2a\xi_i\omega_i + {\omega_i}^2}\right)\sin\left(\omega_i\sqrt{1-{\xi_i}^2} t_1\right) + \frac{k_i P_0}{\omega_i\sqrt{1-{\xi_i}^2}} e^{\xi_i\omega_i t_1}\left(\frac{1 - 2{\xi_i}^2}{t_1{\omega_i}^2} + \frac{a - \xi_i\omega_i}{a^2 - 2a\xi_i\omega_i + {\omega_i}^2} + \frac{\xi_i}{\omega_i}\right)\cos\left(\omega_i\sqrt{1-{\xi_i}^2} t_1\right) \tag{14}$$

Substituting Eqs. (13) and (14) into Eq. (12), and then substituting Eqs. (10) and (12) into Eq. (6), the displacement responses of a cantilever Euler–Bernoulli beam subjected to lateral impact can be obtained.

In the case of considering the effects of shear deformation and rotary inertia terms, the eigenvalue of a cantilever beam $\omega_i^{'}$ based on Timoshenko beam theory is given by

$$\alpha^2\frac{i^4\pi^4}{l^4} - \omega_i^{'2} - \omega_i^{'2}\frac{i^2\pi^2\gamma^2}{l^2} - \omega_i^{'2}\frac{i^2\pi^2\gamma^2}{l^2}\frac{E}{\kappa G} + \frac{\rho\gamma^4}{\kappa G}\omega_i^{'4} = 0 \tag{15}$$

where $\gamma^2 = \frac{I}{A}$, $\alpha^2 = \frac{EI}{m}$, $\rho =$ the density of the beam, $\kappa =$ a constant that accounts for the nonuniform distribution of shear stress across the section and depends on the cross-sectional shape of the beam (e.g., κ is $\frac{5}{6}$ for rectangular cross section and $\frac{9}{10}$ for circular cross section), and $G =$ is the modulus of rigidity.

Neglecting the last two terms of Eq. (15), the eigenvalue of a Euler–Bernoulli cantilever beam ω_i is given by

$$\omega_i = \frac{\alpha i^2\pi^2}{l^2} \tag{16}$$

Substituting Eq. (16) into the last term of Eq. (15), it can be found that the last term of Eq. (15) is much smaller than $\frac{\pi^2 r^2 i^2}{l^2}$, so the last term of Eq. (15) is neglected in calculating the eigenvalue of a cantilever Timoshenko beam, as given by

$$\omega_i^{'} = \omega_i\frac{1}{\sqrt{1 + \left(\frac{i\pi\gamma}{l}\right)^2\left(1 + \frac{E}{\kappa G}\right)}} \tag{17}$$

where $\frac{E}{G} = 2(1+\nu)$ and ν is the Possion's ratio.

Replacing the eigenvalues in Eq. (10) and Eqs. (12)–(14) by Eq. (17), the displacement responses of a cantilever beam subjected to lateral impact can be obtained in which the effects of shear deformation and rotary inertia terms are considered.

5.2. Comparison of analytical and experimental results

The damping ratios of the test specimens are obtained from the logarithmic decrement of displacement histories (Fig. 8). The first three modes are used for the calculation. It is assumed that no delamination between concrete core and outer/inner tubes occurred under impact. The effective bending stiffness of CFFTs $(EI)_{eff}$ is used to predict the displacement responses of test specimens subjected to lateral impact, as given by [20].

$$(EI)_{eff} = \frac{E_f \pi}{4}\left\{\alpha\left[(r+t_1)^4 - r^4\right] + \beta r^4 n\right\} \tag{18}$$

where E_f is Young's modulus of outer FRP tubes, r and t_1 are the inner radius and wall thickness of FRP tubes, and $\alpha = 0.15$ and $\beta = 0.5$ are the reduction factors of FRP and concrete due to impact damage [20], respectively.

Considering the effect of impact damage of FRP and concrete on the bending stiffness of hybrid columns, the concrete area is converted into equivalent the FRP area by applying the modular ratio n, and then the effective bending stiffness of concrete filled FRP-steel DSTCs $(EI)'_{eff}$ is given by [20].

$$(EI)'_{eff} = E_s I_s + \frac{E_f \pi}{4}\left\{\alpha\left[(r_1+t_1+t_2)^4 - (r_1+t_2)^4\right] + \beta n\left[(r_1+t_2)^4 - r_1^4\right]\right\} \tag{19}$$

where E_s and I_s are the Young's modulus and inertia of steel tubes, r_1 and t_2 are the outer radius of steel tubes and wall thickness of concrete, respectively.

The reduction factors of FRP and concrete in the concrete filled FRP-steel DSTCs are deemed as the same as those of in CFFTs. The bending stiffness of steel tubes were not discounted because the no local buckling occurred in the inner steel tubes of concrete filled FRP-steel DSTCs under impact.

Eqs. (18) and (19) were used to calculate the effective bending stiffness of CFFTs and concrete filled FRP-steel DSTCs. Comparisons of the analytical and the measured maximum displacements at the loading point showed good agreement, as given in Table 6.

In the case of the same thickness of GFRP tubes, the intact specimen of concrete filled FRP-steel DSTC has a little higher bending stiffness than the intact specimen of CFFT. After impact, the bending stiffness of CFFT specimens decreased more significantly than that of concrete filled FRP-steel DSTCs, because the inner steel tube was not damaged severely. Hence, the maximum displacement of CFFT specimens was larger than that of concrete filled FRP-steel DSTC specimens under the same applied impact energy.

Table 6

Comparison of maximum displacements between analytical and experimental results.

Specimen	Tested maximum displacement w_1 (mm)	Analytical maximum displacement w_2 (mm)	$\delta = \frac{w_2 - w_1}{w_1} \times$ 100%
C7–I	77.0	70.8	−8.0
C7-II	108.4	100.6	−7.2
C7-III	143.4	135.2	−5.7
C10-III	120.6	115.9	−3.9
D7-I	48.2	44.2	−8.3
D7-II	59.3	54.2	−8.5
D7-III	79.8	75.5	−5.4
D10-III	68.4	65.3	−4.6

6. Conclusions

The structural responses of CFFT and concrete filled FRP-steel DSTC columns under horizontal impact were investigated. The results obtained from this study are summarized as follows:

(1) Circular cracks at the fixed end and crushing of GFRP at the loading point were prevalent in the CFFTs and concrete filled FRP-steel DSTCs. Under the same applied impact energy, the concrete filled FRP-steel DSTCs had more severe damages at the loading point and smaller damage area at the fixed end than CFFTs. Moreover, the maximum and residual lateral deformations of concrete filled FRP-steel DSTCs were much lower than those of CFFTs. It indicated that concrete filled FRP-steel DSTCs had lower local stiffness and higher global stiffness than CFFTs.

(2) Higher impact velocity resulted in higher maximum displacement, higher peak impact force and heavier damage, thus resulting in higher residual deformations. Thicker GFRP tubes resulted in a little increment of peak impact force and a little reduction of duration of both CFFT and concrete filled FRP-steel DSTCs. Moreover, increasing the GFRP thickness led to decrease in maximum displacement and increase in energy absorption for CFFT and concrete filled FRP-steel DSTC specimens. Under the same impact velocity, the concrete filled FRP-steel DSTCs absorbed more energy than CFFTs.

(3) The dynamic analysis program (LS-DYNA) provided reasonable simulation of the experimental results of the impact responses for both hollow and concrete filled GFRP tubes. Moreover, the verified FE model was used to conduct parametric study. It is found that the peak impact load of D7-II decreases by 33%, when the axial compression ratios (ACRs) increase from 0 to 0.6. However, the impact load history of C7-II changed insignificantly with ACRs. Increasing the hollow ratio ϕ of concrete filled FRP-steel DSTCs from 0.3 to 0.6 resulted in 27% decrease of peak impact load and 9% increase of duration. The normal FRP ratio α_f had a more significant influence on the duration than the impact peak load for both CFFTs and concrete filled FRP-steel DSTCs.

(4) The impact force histories were simulated by a dual function. The impact damage of GFRP tubes and concrete were considered in obtaining the effective bending stiffness. Then the Euler -Bernoulli model for lateral displacement of a cantilever beam under impact was used to predict the dynamic displacements. Moreover, the influences of shear deformation and rotary inertia terms on the natural frequencies of the beam were considered. The analytical results agree well with test results.

(5) Under the same applied impact energy and with the same GFRP outer tube, concrete filled FRP-steel DSTCs with hollow ratio of 0.47 have higher impact resistance and energy absorption capacity than CFFTs. Increasing the thickness of GFRP is an effective way to enhance the energy absorption capacity for both CFFTs and concrete filled FRP-steel DSTCs without remarkably increase in the peak impact force. When the columns need to carry heavy axial loads (i.e. ACR = 0.6), CFFTs are more suitable as impact resistance members than concrete filled FRP-steel DSTCs. The brittleness of CFFTs can be improved by internal reinforcement.

Declaration of competing interest

The authors declare that they have no known competing financial interests or personal relationships that could have appeared to influence the work reported in this paper.

CRediT authorship contribution statement

Zhilin Chen: Formal analysis, Validation, Writing - original draft. **Jun Wang:** Investigation, Conceptualization, Formal analysis, Resources. **Jiye Chen:** Writing - review & editing. **Hota GangaRao:** Methodology. **Ruifeng Liang:** Formal analysis. **Weiqing Liu:** Project administration.

Acknowledgments

The financial support from the National Natural Science Foundation of China (Grant No.51578283), Modern Science and Technology Support Program of Jiangsu Construction Industry of China (Grant No. 2016–13) and Top Six Talent Projects in Jiangsu Province, China (Grant No. JZ-024) are greatly appreciated. Partial funding of this research was provided by the U.S. National Science Foundation Grant IIP 1230351.

Appendix A. Supplementary data

Supplementary data to this article can be found online at https://doi.org/10.1016/j.tws.2020.106941.

References

[1] A. Mirmiran, M. Shahawy, A new concrete-filled hollow FRP composite column, Composites Part B 27B (1996) 263–268.
[2] A. Fam, M. Pando, G. Filz, S. Rizkalla, Precast piles for route 40 bridge in Virginia using concrete filled FRP tubes, PCI J. 48 (3) (2003) 32–45.
[3] H.V.S. GangaRao, N. Taly, P.V. Vijay, Reinforced Concrete Design with FRP Composites, Taylor & Francis Group, New York, 2007.
[4] J.G. Teng, T. Yu, Y.L. Wong, S.L. Dong, Hybrid FRP-concrete-steel tubular columns: concept and behavior, Construct. Build. Mater. 21 (4) (2007) 846–854.
[5] L. Lam, J.G. Teng, Design-oriented stress-strain model for FRP-confined concrete, Construct. Build. Mater. 17 (6) (2003) 471–489.
[6] W. Wang, C. Wu, Z. Liu, Compressive behavior of hybrid double-skin tubular columns with ultrahigh performance fiber-reinforced concrete (UHPFRC), Eng. Struct. 180 (2019) 419–441.
[7] H.J. Dagher, D.J. Bannon, W.G. Davids, R.A. Lopez-Anido, E. Nagy, K. Goslin, Bending behavior of concrete-filled tubular FRP arches for bridge structures, Construct. Build. Mater. 37 (2012) 432–439.
[8] T. Yu, Y.L. Wong, J.G. Teng, S.L. Dong, E.S.S. Lam, Flexural behavior of hybrid FRP-concrete-steel double-skin tubular members, J. Compos. Construct. 10 (5) (2006) 443–452.
[9] B. Li, P. Zohrevand, A. Mirmiran, Cyclic behavior of FRP concrete bridge pier frames, J. Bridge Eng. 18 (5) (2013) 429–438.
[10] T.M. Pham, H. Hao, Axial impact resistance of FRP-confined concrete, J. Compos. Construct. 21 (2) (2017), 04016088.
[11] Y. Qasrawi, P.J. Heffernan, A. Fam, Dynamic behaviour of concrete filled FRP tubes subjected to impact loading, Eng. Struct. 100 (2015) 212–225.
[12] L. Huang, X. Sun, L. Yan, B. Kasal, Impact behavior of concrete columns confined by both GFRP tube and steel spiral reinforcement, Construct. Build. Mater. 131 (2017) 438–448.
[13] L. Huang, C. Gao, L. Yan, T. Yu, B. Kasal, Experimental and numerical studies of CFRP tube and steel spiral dual-confined concrete composite columns under axial impact loading, Composites Part B 152 (2018) 193–208.
[14] Y. Xiao, Y. Shen, Impact behaviors of CFT and CFRP confined CFT stub columns, J. Compos. Construct. 16 (6) (2012) 662–670.
[15] M.I. Alam, S. Fawzia, X. Liu, Effect of bond length on the behaviour of CFRP strengthened concrete-filled steel tubes under transverse impact, Compos. Struct. 132 (2015) 898–914.
[16] C. Chen, Y. Zhao, J. Li, Experimental investigation on the impact performance of concrete-filled FRP steel tubes, J. Eng. Mech. 141 (2) (2015), 04014112.
[17] O.I. Abdelkarim, M.A. ElGawady, Performance of hollow-core FRP-concrete-steel bridge columns subjected to vehicle collision, Eng. Struct. 123 (2016) 517–531.
[18] R. Wang, L. Han, Z. Tao, Behavior of FRP-concrete-steel double skin tubular members under lateral impact: experimental study, Thin-Walled Struct. 95 (2015) 363–373.
[19] B. Hobbs, M. Gilbert, T. Molyneaux, Effects of vehicle impact loading on masonry arch parapets, in: Proceeding of the Second International Arch Bridge Conference, Italy, 1998.
[20] J. Wang, H. GangaRao, R. Liang, W. Liu, Experimental and analytical responses of hollow and concrete-filled GFRP tube columns under impact, J. Compos. Construct. 21 (4) (2017), 04017013.
[21] Q. Liu, D. Zhou, J. Wang, W. Liu, Mechanical behavior of FRP confined steel tubular columns under impact, Steel Compos. Struct. 27 (6) (2018) 691–702.
[22] S. Aghdamy, D.P. Thambiratnam, M. Dhanasekar, Experimental investigation on lateral impact response of concrete-filled double-skin tube columns using horizontal-impact-testing system, Exp. Mech. 56 (7) (2016) 1133–1153.
[23] Metallic Materials - Tensile Testing - Part 1: Method of Test at Room Temperature, GB/T 228.1-2010, ISO 6892-1:2009, MOD.
[24] GB, Code for Design of Building Foundations, GB 50007, China Architecture & Building Press, Beijing, China, 2011.
[25] H.V.S. GangaRao, M. Skidmore, Test Report: Concrete Filled Pile, Constructed Facilities Center, West Virginia University, USA, 2014.
[26] Y.D. Murray, Users Manual for LS-DYNA Concrete Material Model 159, Report No. FHWAHRT-05-062, Federal Highway Administration, 2007.
[27] S.D. Adhikary, B. Li, K. Fujikake, Low velocity impact response of reinforced concrete beams: experimental and numerical investigation, Int. J. Prot. Struct. 6 (1) (2015) 81–111.
[28] W. Guo, W. Fan, X. Shao, D. Shen, B. Chen, Constitutive model of ultra-high-performance fiber-reinforced concrete for low-velocity impact simulations, Compos. Struct. 185 (2018) 307–326.
[29] C.M. Hu, L.H. Han, C.C. Hou, Concrete-encased CFST members with circular sections under laterally low velocity impact: analytical behavior, J. Constr. Steel Res. 146 (2018) 135–154.
[30] N.K. Singh, K.K. Singh, Review on impact analysis of FRP composites validated by LS-DYNA, Polym. Compos. 36 (10) (2014) 1786–1798.
[31] W. Wang, C. Wu, J. Li, Z. Liu, X. Zhi, Lateral impact behavior of double-skin steel tubular (DST) members with ultra-high performance fiber-reinforced concrete (UHPFRC), Thin-Walled Struct. 144 (2019) 106351.
[32] W. Wang, C. Wu, J. Li, Z. Liu, Y. Lv, Behavior of ultra-high performance fiber-reinforced concrete (UHPFRC) filled steel tubular members under lateral impact loading, Int. J. Impact Eng. 132 (2019) 103314.
[33] H. Jiang, M.G. Chorzepa, Aircraft impact analysis of nuclear safety-related concrete structures: a review, Eng. Fail. Anal. 46 (2014) 118–133.
[34] R. Wang, L.H. Han, C.C. Hou, Behavior of concrete filled steel tubular (CFST) members under lateral impact: experiment and FEA model, J. Constr. Steel Res. 80 (2013) 188–201.
[35] J.G. Teng, J.F. Chen, S.T. Smith, L. Lam, FRP, Strengthened RC Structures, Wiley, UK, 2002.
[36] GB, Code for Design of Concrete Structure, GB50010, China Architecture & Building Press, Beijing, China, 2015.
[37] T. Yu, B. Zhang, Y.B. Cao, J.G. Teng, Behavior of hybrid FRP-concrete-steel double-skin tubular columns subjected to cyclic axial compression, Thin-Walled Struct. 61 (2012) 196–203.
[38] L.H. Han, G.H. Yao, X.L. Zhao, Tests and calculations for hollow structure steel (HSS) stub columns filled with self-consolidating concrete (SCC), J. Constr. Steel Res. 61 (2005) 1241–1269.
[39] Building Code Requirements for Structural Concrete and Commentary; ACI 318-11, American Concrete Institute (ACI), Farmington Hills, MI, USA, 2011.
[40] L. Brillouin, Wave Propagation and Group Velocity, Academic Press, New York, 1960.
[41] E. Alper, J.I. Daniel, Piezoelectric Energy Harvesting, Appendix C: Modal Analysis of a Uniform Cantilever with a Tip Mass, John Wiley & Sons, 2011.